

Exploring the Magnetic Dynamics of CrMnFeCoNi

Using Muon Spin Relaxation

Emma Zappala

A senior thesis submitted to the faculty of
Brigham Young University
in partial fulfillment of the requirements for the degree of

Bachelor of Science

Ben Frandsen, Advisors

Department of Physics and Astronomy

Brigham Young University

Copyright © 2023 Emma Zappala

All Rights Reserved

ABSTRACT

Exploring the Magnetic Dynamics of CrMnFeCoNi Using Muon Spin Relaxation

Emma Zappala

Department of Physics and Astronomy, BYU
Bachelor of Science

High-entropy alloys are comprised of five or more elements in equal proportions, resulting in a large configurational entropy. The unique composition of these alloys creates properties not observable in conventional materials. While many of these alloys are known to be magnetic, their magnetic properties have not been studied in detail. CrMnFeCoNi, or Cantor alloy, is one of the most well known high-entropy alloys. We used muon spin relaxation, a highly sensitive probe of magnetism, to examine the magnetism of various samples of Cantor alloy, including samples undergoing different treatments in formation and samples with nonequiatomic stoichiometry. The magnetic transition temperature and character of the transition are found to be highly sensitive to the preparation methods and atomic ratios. We also observe significant differences in the spin dynamics depending on the composition. These results set the stage for investigating applications of the magnetic properties of high entropy materials.

Keywords: Muon Spin Relaxation, CrMnFeCoNi, Cantor Alloy, Magnetism, μ SR

ACKNOWLEDGMENTS

Many thanks to Prof. James Hamlin and Timothy Elmslie at the University of Florida for their collaboration on this project. I thank Gerald Morris and Bassam Hitti from the Staff at TRIUMF laboratories for helping with data collection. I would like to thank Dr. Ben Frandsen, who has taught me so much during my time working under him and given me valuable advice that will shape my scientific career. Without him I would not understand any of this material I spent so long researching. I would also like to thank my parents, Daniel and Tracy Zappala, for always encouraging me to follow my dreams.

Contents

Table of Contents	vii
1 Introduction	1
1.1 High Entropy Alloys	1
1.2 Properties and Applications of High Entropy Alloys	3
1.3 CrMnFeCoNi	4
1.4 Magnetic Properties of CrMnFeCoNi	5
2 Methods	7
2.1 Samples	7
2.2 Muon Spin Relaxation	8
2.3 Analysis Software and Techniques	10
3 Results and Discussion	11
3.1 Pristine CrMnFeCoNi	11
3.2 Comparison of Different Samples	14
3.3 Longitudinal Field Data	18
4 Conclusion	23
Bibliography	25

Chapter 1

Introduction

People have sought to develop materials and tools from their environment for as long as they have existed. They are constantly looking for ways to innovate and make their lives more efficient. People learned to make tools from wood, but quickly moved on to metals due to their durability and hardness. They then moved on to improving these materials further by taking a principle element and mixing in other elements to exaggerate their structural qualities. For example, steel is based on Iron mixed with small amounts of Carbon and other elements based on the desired properties [1]. In the 1990s, people moved outside the realm of conventional alloys with a base element and instead mixed many elements in roughly equal, or equiatomic, proportions [2]. Despite the seeming complexity with so many different elements mixed together, the result is a relatively simple structure with numerous useful properties. These alloys were coined as ‘high entropy alloys’ by Yeh et al. [2], due to the high entropy involved in mixing at least five different elements together.

1.1 High Entropy Alloys

Any element made up of five or more elements in roughly equal proportions is classified as a high entropy alloy. When equiatomic multi-element alloys were first discovered, people first turned

to entropy to explain their solid phase at room temperature. Entropy is the measure of disorder in a system. Any spontaneous process that occurs increases the entropy of the universe. The configurational entropy of mixing per mole, or the portion of the entropy of a system that is due to the location of the constituent particles, can be expressed as $\Delta S_{mix} = -R \sum_{i=1}^n c_i \ln c_i$, where R is the gas constant, c_i the molar fraction of the i th element, and n the total number of constituent elements [3]. When the molar fractions become equal, ΔS_{mix} reaches a maximum. For a three element system, the total energy gain $T_m \Delta S_{mix} \sim 20$ kJ/mol with an alloy that has a typical melting point $T_m \sim 2000$ K [4]. This energy gain is sufficient for the entropic stabilization of a random solid solution phase at room temperature [3]. The mixing entropy for an equiatomic high entropy alloy can then be simplified as $\Delta S_{mix} = -R \ln n$. While this is an elegant and simple solution to the explanation of when a solid solution phase will occur, it is not actually correct. It was quickly found that many different phases predicted to be solid at room temperature were not. Experiments found these predicted solid phases to be other phases such as intermetallic compounds and metallic glasses [5–10]. This tells us that ΔS_{mix} cannot be the only factor involved in designing alloys labelled as high entropy alloys.

The missing pieces can be found in two different parameters investigated by Zhang et al. [11], the atomic size difference δ and the mixing enthalpy H_{mix} . The atomic size difference, or just the difference between sizes of the different elements being mixed together, is written as:

$$\delta\% = 100\% \sqrt{\sum_{i=1}^n c_i \left(\frac{1 - r_i}{\sum_{j=1}^n c_j r_j} \right)^2} \quad (1.1)$$

where c_i is the atomic fraction and r_i is the atomic radius of the i th element [11]. The enthalpy, a thermodynamic quantity equivalent to the total heat content of a system, is calculated in high entropy alloys as follows:

$$\Delta H_{mix} = \sum_{i=1, j \neq i}^n \Omega_{ij} c_i c_j = \sum_{i=1, j \neq i}^n 4\Delta H_{ij}^{mix} c_i c_j \quad (1.2)$$

where ΔH_{ij}^{mix} is the enthalpy of mixing of the binary liquid between two elements i and j at an equiatomic composition. High entropy alloys tend to form single-phase solid solutions when there is a low mixing enthalpy and a low atomic size difference [4]. This region tends to be around $-15\text{kJ/mol} < \Delta H_{mix} < 5\text{kJ/mol}$ and $0 < \delta < 5$ [11]. Different phases then appear as these quantities are changed. Looking just at entropy in the way we did earlier assumes that all of the elements have the same size, which will work for situations where that is true, but for most alloys that isn't the case. This two-parameter approach gives a much better prediction of what the phase of the created high entropy alloy will be for any collection of elements.

1.2 Properties and Applications of High Entropy Alloys

Many high entropy alloys have desirable properties for different material applications. Designed high entropy alloys were reported to have superior mechanical and physical properties, including ultrahigh fracture toughness that outperforms that of most pure metals and alloys [12], excellent comparable strength to that of structural ceramics and some metallic glasses [13], superconductivity [14], and significant resistance to corrosion [15].

High entropy alloys are exceptionally hard and have high specific strength. In structural applications such as in aerospace engineering and civil transportations, controlling the weight of any engineering components is essential for reducing the energy demand. There have been many reported low-density and high strength high entropy alloys [13, 16, 17]. Factoring in most high entropy alloy's resistance to corrosion [15] makes high entropy alloys all that much more useful for engineering. Additionally, the high mixing entropy in high entropy alloys at elevated temperatures promotes the formation of single-phase solid solutions, especially at high temperatures [11]. They retain their solid structure for higher temperatures relative to other metals [4]. This makes high entropy alloys useful for mechanical performance at high temperatures due to the sluggish diffusion

of their constituent elements.

In addition to their promising mechanical properties, some high entropy alloys also exhibit useful properties because of their high configurational entropy, which limits precipitation, sometimes even entirely, at a nanometer scale [18]. This ensures that there will be limited, if any, creation of inhomogeneous parts of the sample over time. There have also been reported high entropy alloys with superconducting properties [19]. This suggests that high entropy alloys could be used in strong superconducting electromagnets such as magnetic resonance imaging (MRI) scanners, nuclear magnetic resonance (NMR) machines, and particle accelerators, like several other type II superconductors.

1.3 CrMnFeCoNi

One of the most famous and widely studied high entropy alloys is CrMnFeCoNi. The specific combination of chromium (Cr), manganese (Mn), iron (Fe), cobalt (Co), and nickel (Ni) that would eventually be named “Cantor alloy” was first identified in 2004 by Cantor et al. [21]. CrMnFeCoNi’s atomic structure was identified as face-centered cubic in a wide temperature range [22]. The structure is shown in Figure 1.1. It is highly studied due to its excellent ductility at room temperature [23], making it an excellent example of the superior qualities of high entropy alloys. Cantor alloy also exhibits relatively strong temperature dependence of yield strength

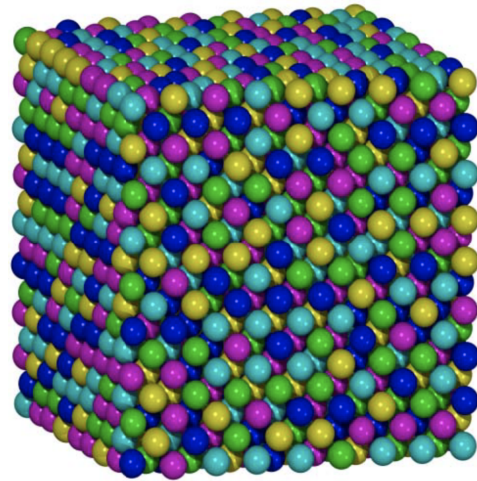


Figure 1.1 The face-centered cubic structure of CrMnFeCoNi. Adapted from Wang et. al [20]

and ductility, with almost a factor of four increase in both as the temperature is decreased from 500 to 77 K [24]. It also has an exceptionally high fracture toughness [25]. In fact, Cantor alloy is among the toughest materials ever known [26]. While much is known about the structure of Cantor alloys, its magnetic properties, and magnetic properties of other high entropy alloys, remain much less well studied.

1.4 Magnetic Properties of CrMnFeCoNi

Cantor alloy is made up of elements that are both antiferromagnetic and ferromagnetic in their individual forms. Of its component elements, Cr and Mn are antiferromagnetic with $T_N = 311\text{K}$ [27] and $T_N = 100\text{K}$ [28], while Fe, Co, and Ni are ferromagnetic with $T_C = 1043\text{K}$, $T_C = 1394\text{K}$, and $T_C = 631\text{K}$, respectively [29]. Cantor alloy was found to have a much lower transition temperature than its constituent elements, though the transition temperature and type of transition have been disputed. In 2016 Jin et al. reported a peak in the magnetization of CrMnFeCoNi at 25 K and suggested that it could be either an antiferromagnetic transition or a spin-glass transition [30], while Schneeweiss et al. found two transitions in the magnetization: a spin-glass transition at 93 K, and a ferromagnetic transition at 38 K [31] in 2017. In 2019 Kamarad et al. observed the magnetic properties over different pressures, finding that increasing pressure decreased magnetization slightly [32]. They also found evidence of strong antiferromagnetic interactions, which they hypothesized were responsible for the observed small magnetization values, as well as the linear field dependence of the magnetization. They also found different transitions, identifying ferrimagnetic order below 85 K and magnetic cluster-glass behavior below 43.5 K. To reconcile these differences in the literature, a comprehensive analysis of CrMnFeCoNi is needed to evaluate what its magnetic properties are. In our experiments we used muon spin relaxation (μSR), a highly sensitive probe to magnetism, to analyze several different Cantor alloy samples with varying preparation methods and compositions.

This technique has not been used to study any high entropy alloys before. Cantor alloy's fame and highly studied structural properties make it an ideal first high entropy alloy to use with (μ SR) techniques.

Chapter 2

Methods

2.1 Samples

We analyzed 5 different samples of Cantor alloy with different preparation techniques and small deviations away from an equiatomic composition. Samples were synthesized by our collaborators at the University of Florida by combining elemental Cr, Mn, Fe, Co, and Ni. They were melted together in an Edmund Buhler MAM-1 compact arc melter [33]. The Cr used for synthesis was 99.995% pure, the Co was 99.5% pure, and all other elements (Mn,Fe,Ni) were 99.95% pure. Three different equiatomic CrMnFeCoNi samples were formed, alongside one CrFeCoNi sample and a sample with excess Mn, $\text{Mn}_{30}(\text{CrFeCoNi})_{70}$. Each sample was melted five times, flipping it over between each melt to improve sample homogeneity. Samples were then sealed in quartz tubes in Ar atmosphere and annealed at 1100 °C for six days, then quenched in water before measurement. One equiatomic CrMnFeCoNi sample created in this way will be referred to as the ‘pristine’ sample, CrFeCoNi as ‘Mn₀’, and $\text{Mn}_{30}(\text{CrFeCoNi})_{70}$ as ‘Mn₃₀’. One equiatomic sample was additionally cold-worked by flattening it in a hydraulic press a total of three times using a pressure of approximately 0.5 GPa, folding it in half between each flattening step. This sample is known as ‘cold-worked’. One

CrMnFeCoNi sample, the ‘premag’ sample, was magnetized with a 9 T field before measurements were taken.

2.2 Muon Spin Relaxation

The data for this experiment was taken using muon spin spectroscopy measurements, or μ SR, a technique that probes the magnetic order and spin dynamics of the material. We conducted our experiments at the TRIUMF Laboratory in Vancouver, British Columbia using the LAMPF spectrometer on the M20D beamline, shown in Figure 2.1. The samples were mounted on a low background copper sample holder, and the temperature controlled using a helium gas flow



Figure 2.1 M20D beamline located at TRIUMF Laboratory in Vancouver, British Columbia

cryostat. μ SR relies on the muon, a unique subatomic particle whose spin and charge are exquisitely sensitive local magnetic and electronic probes of matter. A source of protons collided with a light element (for example, carbon or beryllium) creates a pion, which then decays into a muon and a neutrino. Because of parity violation, the created beam of muons are spin polarized opposite to their momentum, so a beam of muons created in this way is essentially polarized in one direction [34].

The created muon will then travel down into a sample, starting an electronic timing circuit before it enters, where it will experience the local magnetic field of wherever it stops within the material. The muon undergoes Larmor precession in the local magnetic field at its position. When the muon decays it emits a positron preferentially along the new spin direction, again due to parity violation [34]. A pair of positron detectors is placed on either side of the sample to detect the

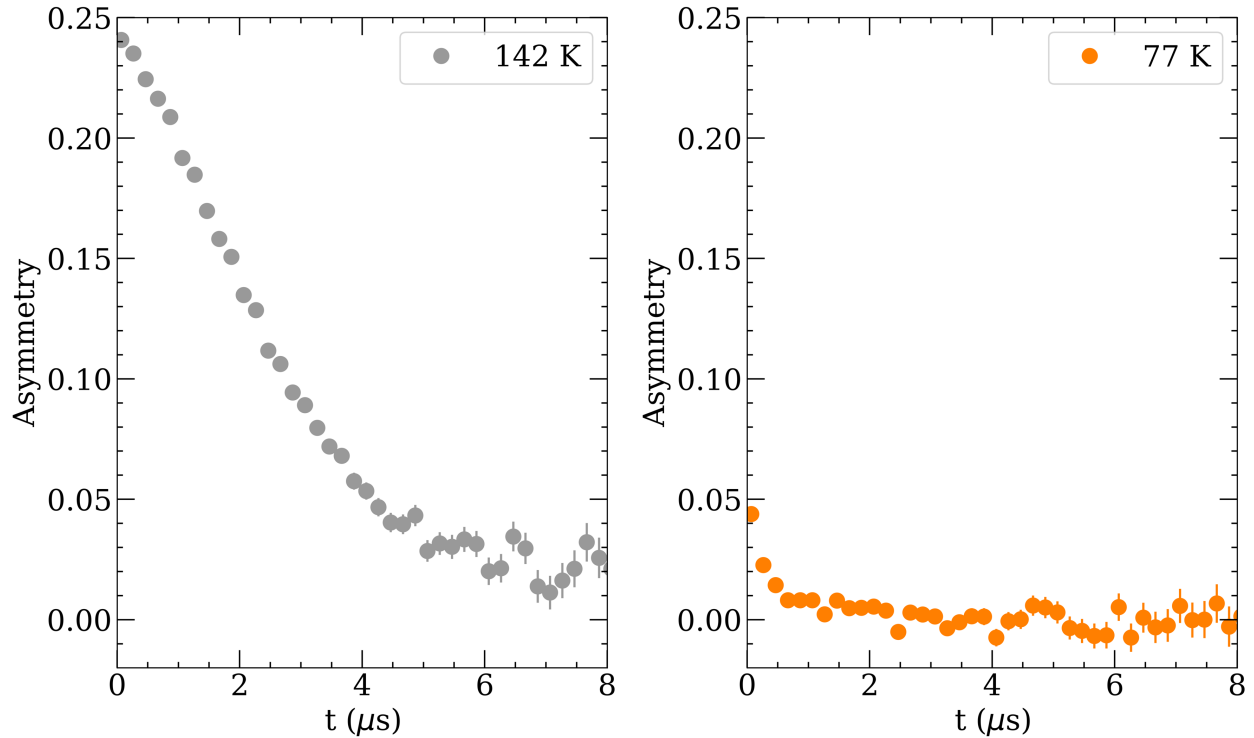


Figure 2.2 Example spectra from a μ SR run for Pristine CrMnFeCoNi. The left is a run at 142K above the magnetic transition, while the right is a run at 77 K below the transition.

emitted positrons. A positron decay event registered by a detector stops the timing circuit, and the elapsed time since muon implantation is recorded. The main experimental quantity determined in a μ SR experiment is the time-dependent asymmetry, defined as $a(t) = [N_1(t) - N_2(t)]/[N_1(t) + N_2(t)]$ where N_1 and N_2 are the number of positron events recorded at a time t in front of and behind the beam respectively, gives the projection of the muon ensemble spin polarization along the axis defined by the positions of the detectors, or the asymmetry of the beam over time [35]. Millions of positron events are typically recorded for each measurement, which usually takes between 30 minutes and an hour. The rate of depolarization of the muon beam, or relaxation, over time can help us infer information about the magnetic field of the material. By repeating this over several temperatures and different applied fields we can paint a picture of how the magnetic dynamics

change over temperature. Figure 2.2 shows an example of two different μ SR runs above and below the magnetic transition. At 142 K the initial asymmetry is at ~ 0.25 , a typical value for 100% polarization in the sample. As time progresses however, the muons have more and more time to experience the local magnetic field, in this case nuclear dipole fields, and the asymmetry level goes down, or relaxes into an unpolarized state. At 77 K, after the magnetic transition has occurred, we see the same behavior but on a much shorter timescale. The beam becomes completely depolarized, or relaxed, before 1 μ s has passed, as opposed to $\sim 6 \mu$ s for 142 K, above the transition.

2.3 Analysis Software and Techniques

We analyzed the data from these μ SR experiments using the open source software BEAMS, which was created by Alec Petersen and Jared Black at Brigham Young University as an easy and accessible way to fit μ SR data. BEAMS is a python based program that uses SciPy to create non-linear least squares fits based on a user provided fitting function for a set of data [36]. It also provides a view of the integrated asymmetry for each temperature point in a specified range of different sets of μ SR runs, giving a good initial view into what the data is doing.

Chapter 3

Results and Discussion

3.1 Pristine CrMnFeCoNi

Figure 3.1 shows a selection of zero field runs featuring overarching important features found in the μ SR data between 2 K and 153 K. At the highest temperatures studied, the relaxation features a gentle Gaussian-like curve. As the temperature decreases the relaxation rate increases and becomes more exponential. The initial asymmetry drops between ~ 0.24 and ~ 0.135 at 87 K and 82 K respectively, and then drops again to ~ 0.08 at 77 K. At this point the initial asymmetry stays around this spot, about 1/3 of the total asymmetry. This well known ‘1/3 tail’, is the sign of a polycrystalline material with static magnetism throughout the whole sample. The lack of oscillations in the ‘2/3 component’ suggests very large fields and/or a broad distribution of field strengths at muon stopping sites [37]. As the temperature lowers further than 77 K the long term relaxation gradually slows, until we see a flat line with no relaxation of the ‘1/3 component’ at 2 K. This is consistent with the magnetic fluctuations freezing out.

Least squares fits from BEAMS, also shown in Figure 3.1 for selected temperatures, were created using a stretched exponential function, $a(t) = a_0 e^{-(\lambda t)^\beta}$, where $a(t)$ is the time dependent

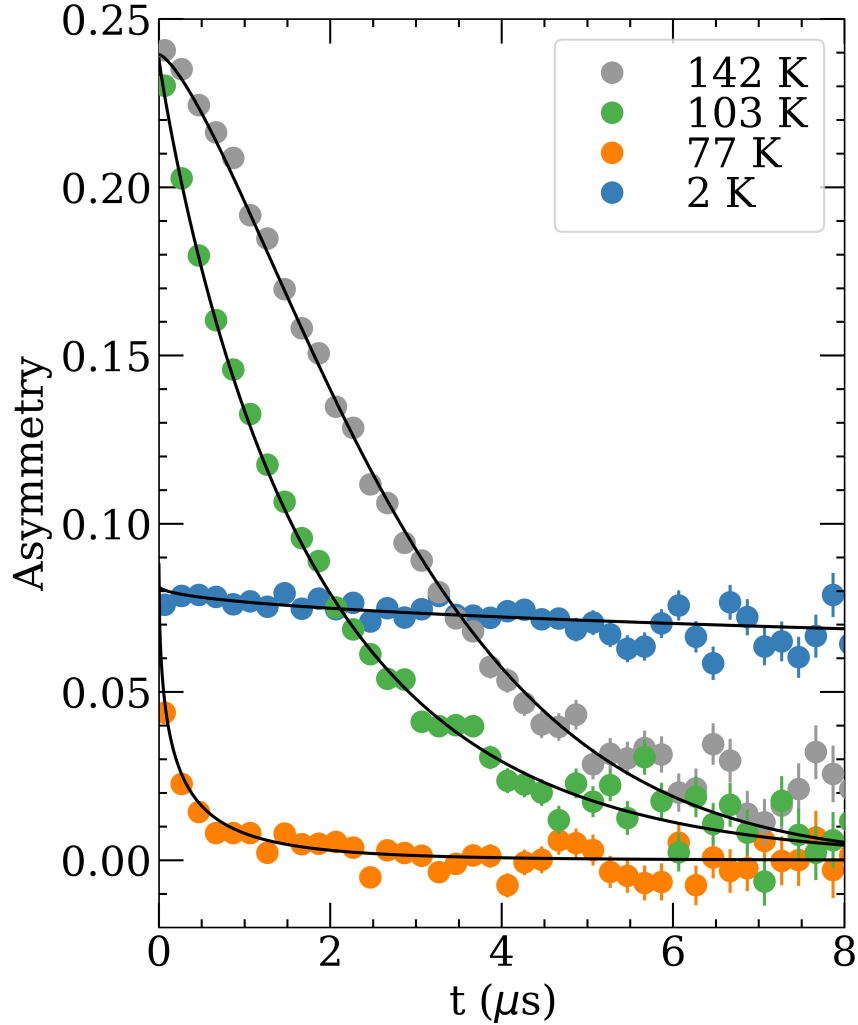


Figure 3.1 Representative spectra of zero field data for pristine CrMnFeCoNi. Dots mark the asymmetry of the positrons, and therefore the muon beam, at that specific point in time. The black line is the fitted time dependence for the respective temperature.

asymmetry, a_0 is the initial asymmetry at $t = 0$, λ is the relaxation rate, and β is the exponential power. This type of relaxation is a typical equation used to model a continuous distribution of relaxation rate [38]. The best fit lines agree with the distribution of the data, as seen in Figure 3.1. The different parameters, shown in figure 3.2, also tell us information about the magnetic dynamics in Cantor alloy. Qualitatively, it is clear that a transition that is sharp and uniform happens between

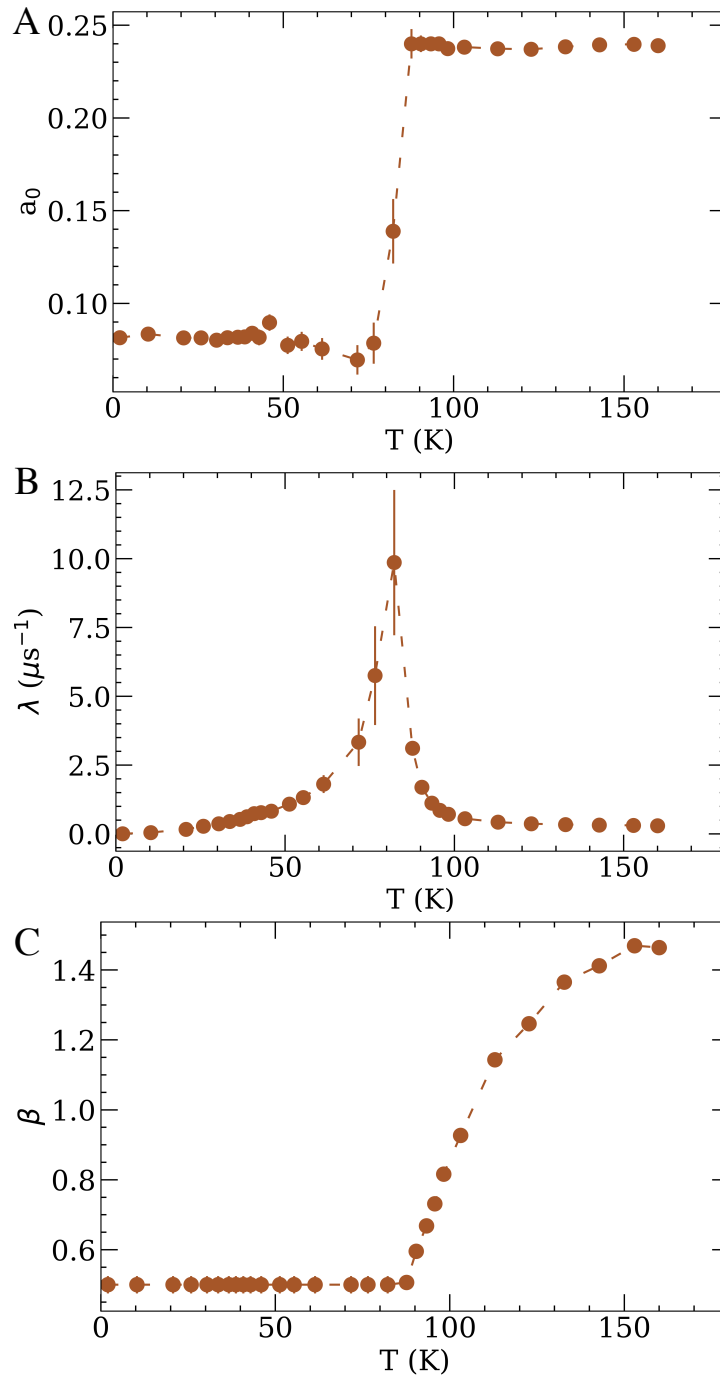


Figure 3.2 The fitting parameters for Pristine CrMnFeCoNi for the equation $a(t) = a_0 e^{-(\lambda t)^\beta}$. Figure A is a_0 , the initial asymmetry over temperature, figure B is λ , the relaxation rate for each temperature, and figure C is β , the exponential power for each temperature.

82 K and 87 K. No transition is clear around 43 K, the proposed second transition, so a transition at this temperature is not due to a minority phase in the sample, or we would see another drop of asymmetry at this temperature. In Figure 3.2 A, we see the sharp drop in the initial asymmetry, showing that the sample undergoes a highly uniform magnetic transition. This is also shown in figures 3.2 B and C. There is a prominent peak in the relaxation rate λ centered around 82 K, an evidence of critical spin dynamics as the temperature approaches the transition, a phenomenon observed in canonical spin glasses and continuous phase transitions [39,40]. The exponential power β peaks at ~ 1.5 at high temperature where relaxation from nuclear dipole fields is the strongest field, and β decreases as temperature is lowered and the electronic spin fluctuations become stronger, and their influence is more prominent. The β value reaches a minimum at the transition around 82 K. Left alone the β value hovers around 0.45 and 0.55, but for consistency we fixed it to 0.5 for the spectra collected at 82 K and below. This is because 0.5 is the value expected for a system that exhibits multiple different relaxation channels and/or spin fluctuation rates [41]. This behaviour would be typical of a material with such high disorder, like Cantor alloy. A similar behavior was observed in the past with an alloy of similar disorder, (Mg,Co,Ni,Cu,Zn)O [42].

3.2 Comparison of Different Samples

Now we expand our view out to the differing samples of Cantor alloy. Representative spectra for all the different samples are shown in Figure 3.3. It is clear that the samples' transition temperatures are different just from comparing these different spectra to each other. The well known '1/3 tail' is also present in these four samples. This confirms that there is the sign of a polycrystalline material with static magnetism throughout the whole sample for each type of Cantor alloy [37], showing that even deviations from an equiatomic Cantor alloy preserves a static magnetic field. However, just comparing these spectra against each other does not provide a very accurate general analysis

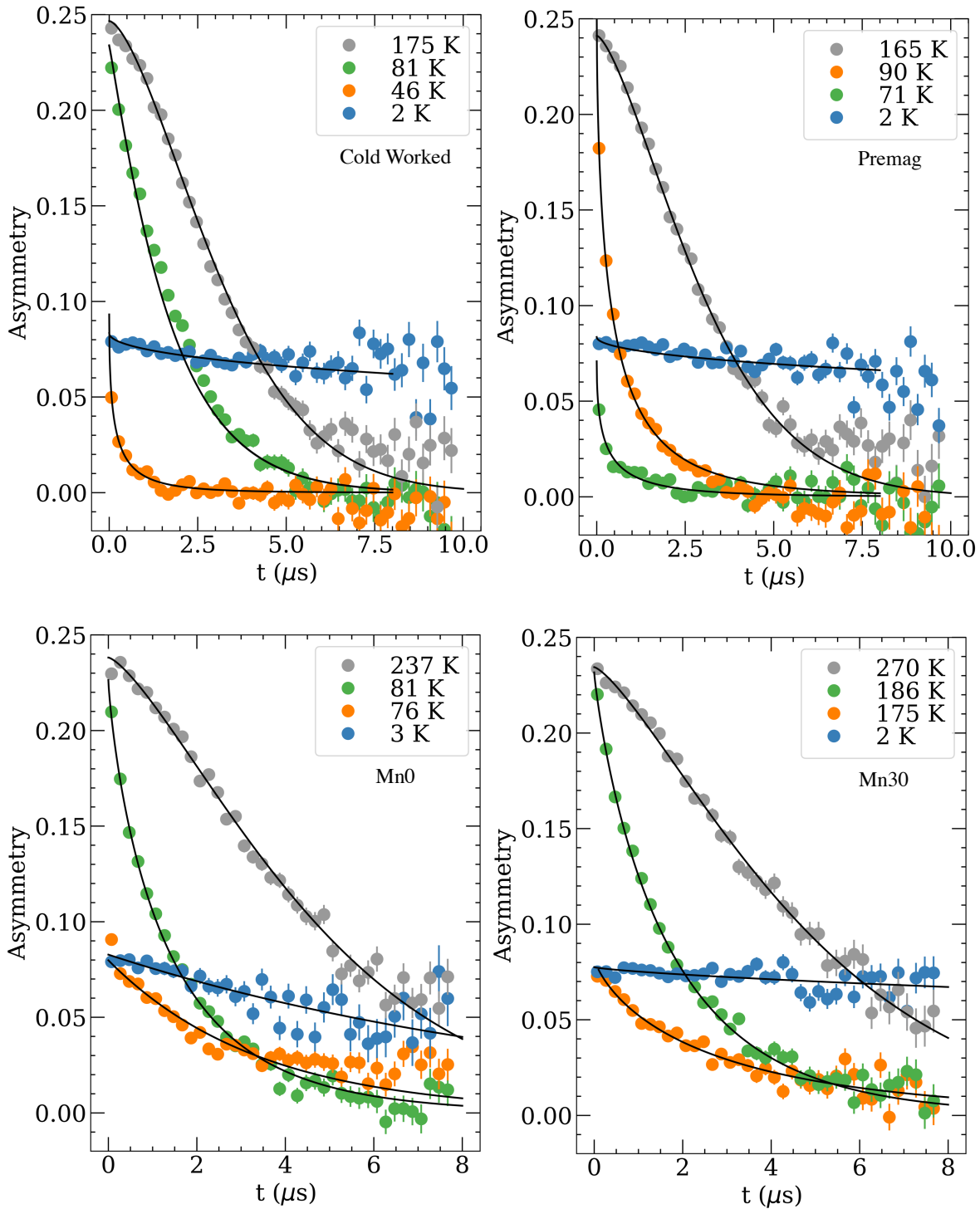


Figure 3.3 Representative spectra for each of the remaining samples of CrMnFeCoNi. Each spectra is labels with its respective sample. Dots mark the asymmetry of the positrons, and therefore the muon beam, at that specific point in time. The black line is the fitted time dependence for the respective temperature.

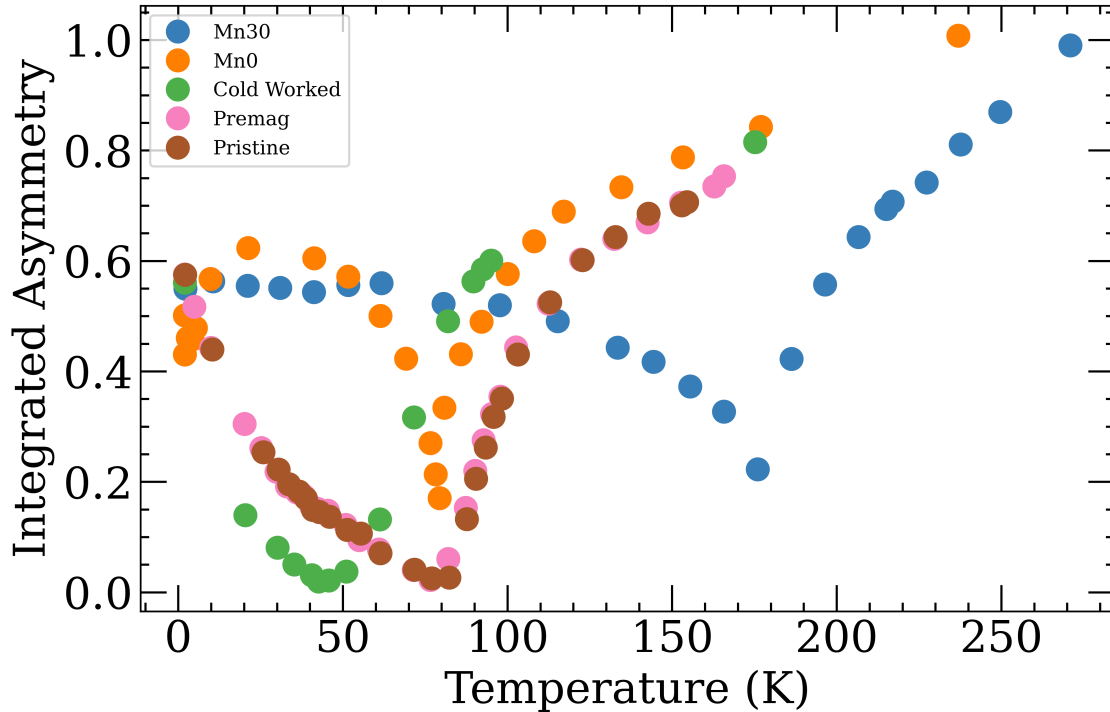


Figure 3.4 The Integrated Asymmetry for each sample. Each point on this graph corresponds to the average total relaxation over all time for that temperature point and sample.

of differences and similarities for these different materials. It is useful to look at the integrated, or average, asymmetry when comparing many different samples to each other. Figure 3.4 shows the integrated asymmetry for all five samples. The simplicity of this graph allows for easy comparison of the different samples. The lowest point for each color is where the relaxation point is the fastest, and therefore where the transition occurs for that sample. It is clear from this graph that the pristine and premag samples have indistinguishable transitions between 82 K and 87 K. The cold worked sample seems to have a lower transition, at ~ 50 K, Mn_{30} has a higher transition temperature at ~ 175 K and while the Mn_0 sample has a slightly lower transition temperature of ~ 78 K.

The same fitting equation, $a(t) = a_0 e^{-(\lambda t)^\beta}$, was used in the fitting software BEAMS for these samples. The individual parameters for each sample are shown in Figure 3.5. In Figure 3.5 A, we see the sharp drop in the initial asymmetry, for every sample except the cold worked, showing that

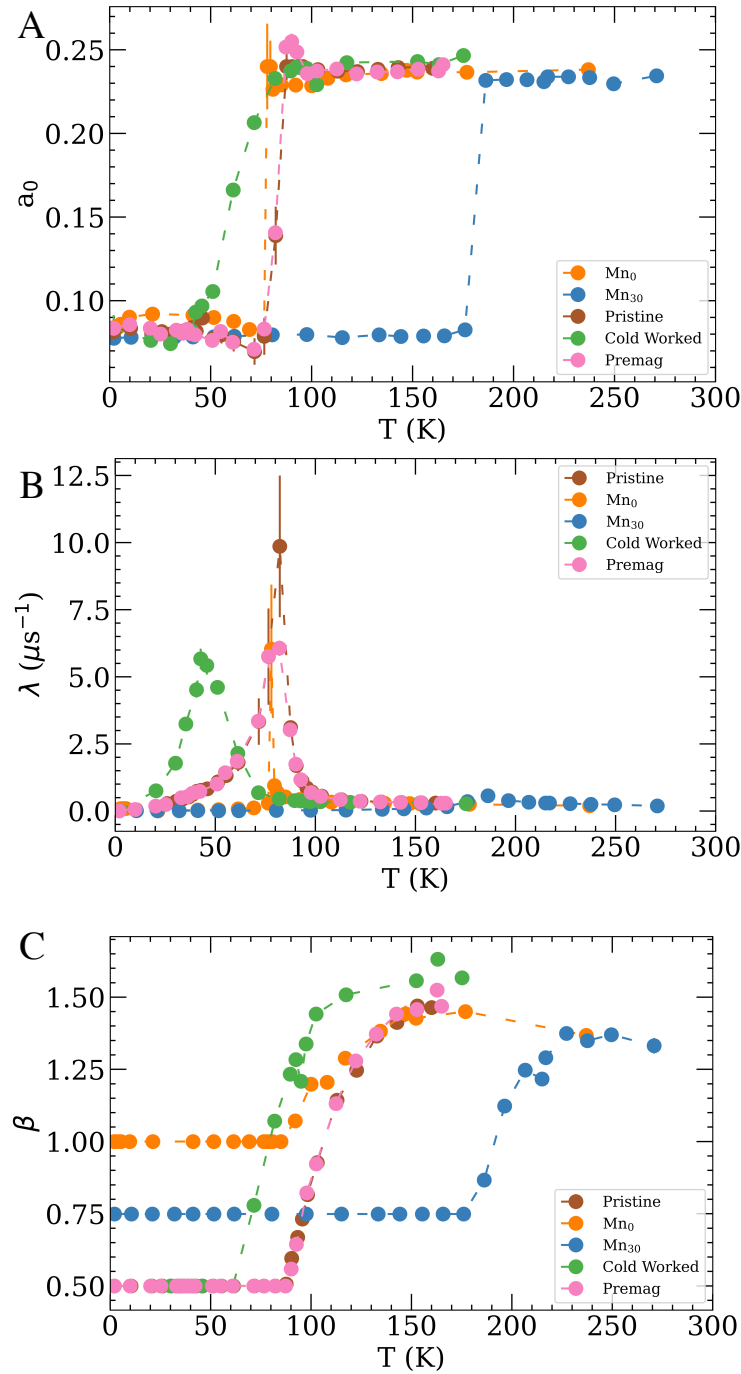


Figure 3.5 The fitting parameters for all samples of CrMnFeCoNi and its variations for the equation $a(t) = a_0 e^{-(\lambda t)^\beta}$. Figure A is a_0 , the initial asymmetry over temperature, figure B is λ , the relaxation rate for each temperature, and figure C is β , the exponential power for each temperature.

these samples also undergo a highly uniform magnetic transition. The cold worked also features a drop in asymmetry, but over a wider temperature range, between 82 K and 41 K. This is indicative of a broader less uniform transition. Different parts of the sample may be transitioning before others causing the asymmetry to drop in some parts of the sample before others, causing a more sloped transition overall. There is also the prominent peak in the relaxation rate λ centered around 82 K, for pristine and premag, 78 K for Mn₀, and 186 K for Mn₃₀, also showing evidence of critical spin dynamics as the temperature approaches the transition, as observed in canonical spin glasses and continuous phase transitions [39,40]. However, the peak in the Mn₃₀ sample is much smaller in magnitude, so the spin dynamics are not quite as pronounced. The cold worked also features a peak around 43 K, though this peak is much wider. This indicates that the critical spin dynamics are suppressed in this sample compared to the others.

The β values for these samples vary. The Mn₀ sample exhibits the normal behavior. A β value of 1 indicates one major spin relaxation mechanism. The cold worked, premag, and pristine samples all fall to that 0.5 value, expected for a system that exhibits multiple different relaxation channels and/or spin fluctuation rates [41]. We fixed Mn₃₀ to ~ 0.75 below the transition, where most of the values we hitting in that temperature range, due to a large amount of scattering in the data. When fixed it is much easier to compare the relaxation rate, λ , which has much more physical significance.

3.3 Longitudinal Field Data

We also took data with a 1 kOe field applied parallel to the initial muon spin direction. Resultant spectra (not shown) reflect a similar pattern to the Zero Field data in general shape. The data was fit with the same stretched exponential, $a_{LF}(t) = a_0 e^{-\lambda_{LF} t^\beta}$. Figure 3.6 A shows the initial asymmetry a_0 . The only abnormal thing about the initial asymmetry is found in the Mn₀ sample, which features a slope between ~ 120 K and ~ 50 K where a_0 decreases instead of the sharp drop characteristic

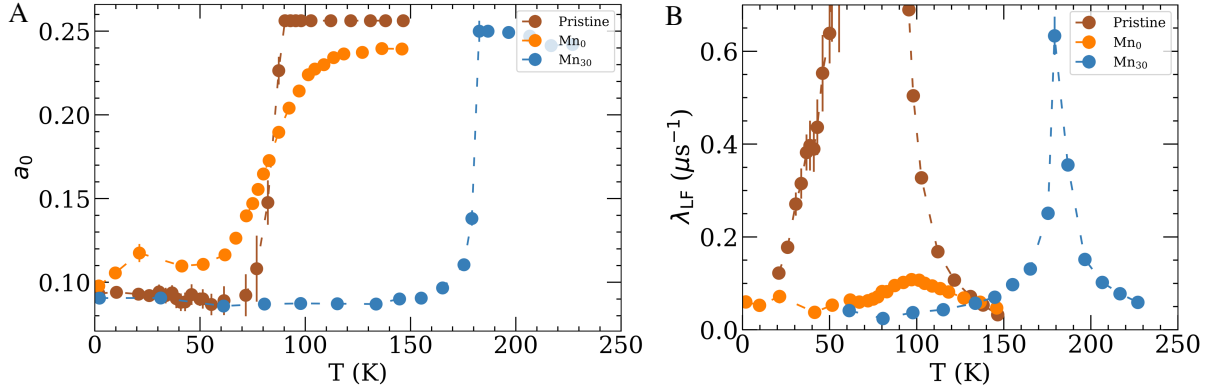


Figure 3.6 The fitting parameters a_0 and λ_{LF} from the fitting the equation $a_{LF}(t) = a_0 e^{-\lambda_{LF} t}$ for Longitudinal Field data for the pristine, Mn₀, and Mn₃₀ samples. The Pristine λ_{LF} goes off the graph for the purpose of showing the peak in the Mn₀ data.

of a uniform magnetic transition, indicating that the transition is not uniform when a field is applied (in contrast to the zero field situation). Figure 3.6 B outlines the long time relaxation rate λ_{LF} . The pristine sample features a peak around the same transition temperature 82 K, not shown in its entirety due to the smaller peaks featured by the Mn₃₀ and Mn₀. The Mn₃₀ sample has a sharp peak in λ_{LF} centered around 183 K, slightly lower than the Zero Field transition centered around 186 K. The Mn₀ features a slightly higher peak than its Zero Field counterpart, at 97 K instead of 78 K. The peak is also significantly smaller and much broader than the Zero Field peak. The difference in these two peaks shows that there are differences in the spin dynamics between the two materials; Mn₃₀ retains its critical spin dynamics in an applied field, while Mn₀ loses it. Mn₀ also exhibits a behavior not seen in any other sample. In the short term relaxation, before $\sim 0.2 \mu\text{s}$ have passed, we observe a Kubo-Toyabe relaxation pattern [43]. This behavior is not visible in a long timescale view. This is just another way that Mn₀ is different from the other materials, showing there are subtle changes in the magnetic field distribution for different compositions of Cantor alloy.

In a system with a single relaxation channel and a spin fluctuation rate ν in the paramagnetic

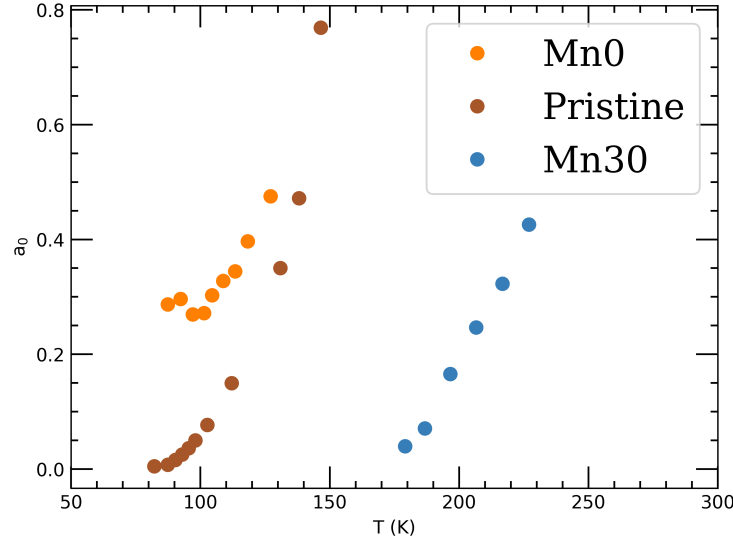


Figure 3.7 The resulting calculation for ν , the spin fluctuation. The decrease approaching the respective transition temperature for each sample is characteristic of the critical slowing down of the spin fluctuations as the transition is approached.

phase, the relaxation rate λ_{LF} is related to ν in the following way [40]

$$\nu = \frac{\Delta^2 + \sqrt{\Delta^4 - \lambda^2 * \omega_L^2}}{\lambda}, \quad (3.1)$$

where $\Delta = \gamma_\mu B_i$ is the product of the rms internal field B_i and the muon's gyromagnetic ratio, and $\omega_L = \gamma_\mu B_L$ is the Larmor frequency of the muon spin in the longitudinally applied field B_L . Since Δ , λ , and ω_L values are experimentally determined, ν can be calculated. Δ can be estimated from the Kubo-Toyabe behavior exhibited by Mn₀, and λ the λ_{LF} found in fitting the longitudinal field data. Figure 3.7 shows the resultant ν for each of the samples with longitudinal field data, pristine, Mn₀ and Mn₃₀. The decrease in each of these as they approach their respective transition temperatures shows the critical slowing of the spin fluctuations approaching the transition.

The decrease of λ as the temperature is raised away from the transition is a result of the thermal activation of spin flip processes and is modeled by [44]

$$\lambda_{LF}(T) = \lambda_0 \exp(E_a/k_B T), \quad (3.2)$$

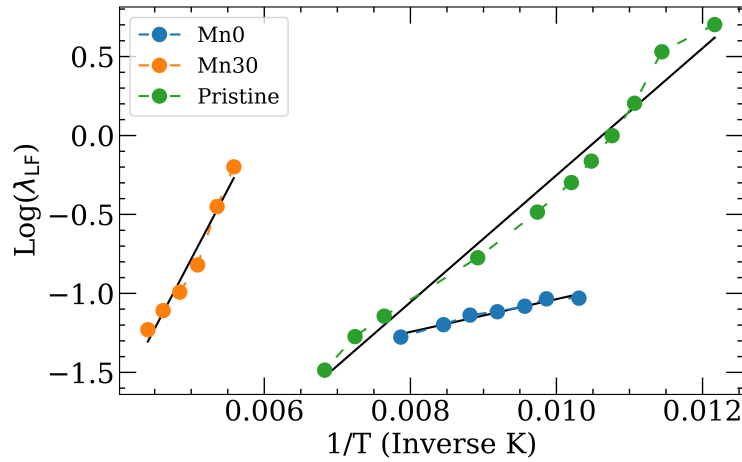


Figure 3.8 This graph shows the relaxation rate λ_{LF} in log space and plots it by its inverse temperature. This gives a view of the thermal activation energy.

where T is the temperature, E_A is the activation energy for flipping a spin, k_B is the Boltzmann constant, and λ_0 is an intrinsic relaxation rate. Figure 3.8 shows λ_{LF} in log space and plots it by its inverse temperature. Since we see a linear relationship in logspace, the slope of this graph is E_A/k_B . The thermal activation energy E_A is 1.43×10^{-21} J for Mn0, 1.21×10^{-20} J for Mn0, and 5.55×10^{-21} J for the pristine sample. A best fit line for each is shown in Figure 3.8.

Chapter 4

Conclusion

This work solidifies our knowledge of the magnetic properties of Cantor alloy, and begins to speculate on how changes in preparation and stoichiometry may effect those properties. μ SR measurements indicate a spin-glass transition around 82 K for pristine CrMnFeCoNi. The transition is homogeneous. This transition is highly sensitive to cold working, and possibly other forms of treatment. The cold worked sample of CrMnFeCoNi features a transition around 78 K that is not homogeneous. The initial asymmetry points to different parts of the material becoming magnetically ordered sooner than others. This may be because cold working disrupts the homogeneous structure of Cantor alloy, creating bigger pockets of Fe or Mn that become magnetically ordered before or after the rest of the sample, causing the asymmetry to drop in some parts of the sample before others. This would be averaged out over the whole sample creating the slope like behavior we see in the initial asymmetry of the cold worked sample. We could do Scanning Electron Microscopy (SEM), Transmission electron microscopy (TEM), or use some other structure probing tool to confirm this. The spin glass transition also depends on the chemical composition of Cantor alloy. The transition temperature of Mn₃₀ is around 182 K, higher than the equiatomic sample. The Mn₀ sample has also has a higher transition temperature than the pristine sample, around 97 K. There would have to be more research to determine the relationship between the composition and the transition temperature.

Departing from equiatomic Cantor alloy also may change the homogenetic nature of the transition. When subjected to a magnetic field, a homogeneous transition is preserved in the Mn₃₀ sample, but is lost in the Mn₀ sample. Further research would have to be done to make any concrete statement about the nature of this change.

There is a definite relationship of the composition of Cantor alloy and the thermal activation energy of the material. The thermal activation energy of equiatomic CrMnFeCoNi is 5.55×10^{-21} J, while the Mn₀ and Mn₃₀ lies below and above that, respectively. Further research would define a quantitative relationship between these values if it was needed to tune the thermal activation energy to a specific value.

This work provides a valuable foundation of experimental results regarding the magnetic properties of Cantor alloy and its derivatives. The dependence of important magnetic parameters on sample composition and preparation suggests that applications of Cantor alloy with tunable magnetic properties may be possible in the future.

Bibliography

- [1] M.-H. Tsai and J.-W. Yeh, “High-entropy alloys: a critical review,” *Materials Research Letters* **2**, 107–123 (2014).
- [2] J.-W. Yeh, S.-K. Chen, S.-J. Lin, J.-Y. Gan, T.-S. Chin, T.-T. Shun, C.-H. Tsau, and S.-Y. Chang, “Nanostructured High-Entropy Alloys with Multiple Principal Elements: Novel Alloy Design Concepts and Outcomes,” *Advanced Engineering Materials* **6**, 299–303 (2004).
- [3] R. A. Swalin and J. Arents, “Thermodynamics of solids,” *Journal of The Electrochemical Society* **109**, 308C (1962).
- [4] Y. Ye, Q. Wang, J. Lu, C. Liu, and Y. Yang, “High-entropy alloy: challenges and prospects,” *Materials Today* **19**, 349–362 (2016).
- [5] A. Takeuchi, K. Amiya, T. Wada, K. Yubuta, and W. Zhang, “High-entropy alloys with a hexagonal close-packed structure designed by equi-atomic alloy strategy and binary phase diagrams,” *Jom* **66**, 1984–1992 (2014).
- [6] O. Senkov, G. Wilks, D. Miracle, C. Chuang, and P. Liaw, “Refractory high-entropy alloys,” *Intermetallics* **18**, 1758–1765 (2010).
- [7] O. Senkov, J. Miller, D. Miracle, and C. Woodward, “Accelerated exploration of multi-principal element alloys with solid solution phases,” *Nature communications* **6**, 6529 (2015).

- [8] J. He, W. Liu, H. Wang, Y. Wu, X. Liu, T. Nieh, and Z. Lu, "Effects of Al addition on structural evolution and tensile properties of the FeCoNiCrMn high-entropy alloy system," *Acta Materialia* **62**, 105–113 (2014).
- [9] H. Ding and K. Yao, "High entropy Ti₂₀Zr₂₀Cu₂₀Ni₂₀Be₂₀ bulk metallic glass," *Journal of non-crystalline solids* **364**, 9–12 (2013).
- [10] K. Guan-Yu, C. Swe-Kai, H. Tung, and Y. Jien-Wei, "FCC and BCC equivalents in as-cast solid solutions of Al [x] Co [y] Cr [z] Cu [0.5] Fe [v] Ni [w] high-entropy alloys," Cachan, France p. 669 (2006).
- [11] Y. Zhang and Y.-n. Lv, "On the nonisospectral modified Kadomtsev–Pevashvili equation," *Journal of mathematical analysis and applications* **342**, 534–541 (2008).
- [12] B. Gludovatz, A. Hohenwarter, D. Catoor, E. H. Chang, E. P. George, and R. O. Ritchie, "A fracture-resistant high-entropy alloy for cryogenic applications," *Science* **345**, 1153–1158 (2014).
- [13] K. Youssef and S. R. Roberto, "Applications of salt solutions before and after harvest affect the quality and incidence of postharvest gray mold of 'Italia' table grapes," *Postharvest Biology and Technology* **87**, 95–102 (2014).
- [14] P. Koželj, S. Vrtnik, A. Jelen, S. Jazbec, Z. Jagličić, S. Maiti, M. Feuerbacher, W. Steurer, and J. Dolinšek, "Discovery of a superconducting high-entropy alloy," *Physical review letters* **113**, 107001 (2014).
- [15] C. Lee, Y. Chen, C. Hsu, J. Yeh, and H. Shih, "The effect of boron on the corrosion resistance of the high entropy alloys Al₁₀.5CoCrCuFeNiB_x," *Journal of the Electrochemical Society* **154**, C424 (2007).

- [16] O. N. Senkov, S. V. Senkova, C. Woodward, and D. B. Miracle, “Low-density, refractory multi-principal element alloys of the Cr–Nb–Ti–V–Zr system: Microstructure and phase analysis,” *Acta Materialia* **61**, 1545–1557 (2013).
- [17] N. Stepanov, D. Shaysultanov, G. Salishchev, and M. Tikhonovsky, “Structure and mechanical properties of a light-weight AlNbTiV high entropy alloy,” *Materials Letters* **142**, 153–155 (2015).
- [18] X. Xu, P. Liu, S. Guo, A. Hirata, T. Fujita, T. Nieh, C. Liu, and M. Chen, “Nanoscale phase separation in a fcc-based CoCrCuFeNiAl_{0.5} high-entropy alloy,” *Acta Materialia* **84**, 145–152 (2015).
- [19] X. Wang, Y. Zhang, Y. Qiao, and G. Chen, “Novel microstructure and properties of multicomponent CoCrCuFeNiTi_x alloys,” *Intermetallics* **15**, 357–362 (2007).
- [20] S. Wang, “Atomic structure modeling of multi-principal-element alloys by the principle of maximum entropy,” *Entropy* **15**, 5536–5548 (2013).
- [21] B. Cantor, I. Chang, P. Knight, and A. Vincent, “Microstructural development in equiatomic multicomponent alloys,” *Materials Science and Engineering: A* **375**, 213–218 (2004).
- [22] T. Zhang, L. Xin, F. Wu, R. Zhao, J. Xiang, M. Chen, S. Jiang, Y. Huang, and S. Chen, “Microstructure and mechanical properties of Fe_xCoCrNiMn high-entropy alloys,” *Journal of Materials Science & Technology* **35**, 2331–2335 (2019).
- [23] G. Salishchev, M. Tikhonovsky, D. Shaysultanov, N. Stepanov, A. Kuznetsov, I. Kolodiy, A. Tortika, and O. Senkov, “Effect of Mn and V on structure and mechanical properties of high-entropy alloys based on CoCrFeNi system,” *Journal of Alloys and Compounds* **591**, 11–21 (2014).

- [24] E. P. George, W. Curtin, and C. C. Tasan, “High entropy alloys: A focused review of mechanical properties and deformation mechanisms,” *Acta Materialia* **188**, 435–474 (2020).
- [25] B. Gludovatz, A. Hohenwarter, K. V. Thurston, H. Bei, Z. Wu, E. P. George, and R. O. Ritchie, “Exceptional damage-tolerance of a medium-entropy alloy CrCoNi at cryogenic temperatures,” *Nature communications* **7**, 10602 (2016).
- [26] W. Li, P. K. Liaw, and Y. Gao, “Fracture resistance of high entropy alloys: A review,” *Intermetallics* **99**, 69–83 (2018).
- [27] G. Bacon and N. Cowlam, “Magnetic studies of annealed and alloyed chromium by neutron diffraction,” *Journal of Physics C: Solid State Physics* **2**, 238 (1969).
- [28] L. Patrick, “Antiferromagnetism of manganese,” *Physical Review* **93**, 370 (1954).
- [29] J. R. Rumble, “CRC Handbook of Chemistry and Physics, 102nd ed.,” (2021).
- [30] K. Jin, B. C. Sales, G. M. Stocks, G. D. Samolyuk, M. Daene, W. J. Weber, Y. Zhang, and H. Bei, “Tailoring the physical properties of Ni-based single-phase equiatomic alloys by modifying the chemical complexity,” *Scientific reports* **6**, 20159 (2016).
- [31] O. Schneeweiss *et al.*, “Magnetic properties of the CrMnFeCoNi high-entropy alloy,” *Physical Review B* **96**, 014437 (2017).
- [32] J. Kamarád, M. Friák, J. Kaštil, O. Schneeweiss, M. Šob, and A. Dlouhý, “Effect of high pressure on magnetic properties of CrMnFeCoNi high entropy alloy,” *Journal of Magnetism and Magnetic Materials* **487**, 165333 (2019).
- [33] T. A. Elmslie *et al.*, “Magnetic properties of equiatomic CrMnFeCoNi,” *Physical Review B* **106**, 014418 (2022).
- [34] J. E. Sonier, “Muon Spin Rotation/Relaxation/Resonance,” (2002).

- [35] S. Blundell, “Spin-polarized muons in condensed matter physics,” *Contemporary Physics* **40**, 175–192 (1999).
- [36] K. A. Petersen and J. Black, “BEAMS,” <https://github.com/FrandsenGroup/beams> (2022).
- [37] S. L. Lee, R. Cywinski, and S. Kilcoyne, *Muon science: Muons in physics, chemistry and materials* (CRC press, 1999), Vol. 51.
- [38] M. Crook and R. Cywinski, “Voigtian Kubo-Toyabe muon spin relaxation,” *Journal of Physics: Condensed Matter* **9**, 1149 (1997).
- [39] A. Yaouanc and P. D. De Reotier, *Muon spin rotation, relaxation, and resonance: applications to condensed matter* (Oxford University Press, 2011), No. 147.
- [40] Y. Uemura, i. T. Yamazaki, n. D. Harshman, M. Senba, and E. Ansaldo, “Muon-spin relaxation in AuFe and CuMn spin glasses,” *Physical Review B* **31**, 546 (1985).
- [41] S. Dunsiger *et al.*, “Muon spin relaxation investigation of the spin dynamics of geometrically frustrated antiferromagnets $Y_2Mo_2O_7$ and $Tb_2Mo_2O_7$,” *Physical Review B* **54**, 9019 (1996).
- [42] B. A. Frandsen, K. A. Petersen, N. A. Ducharme, A. G. Shaw, E. J. Gibson, B. Winn, J. Yan, J. Zhang, M. E. Manley, and R. P. Hermann, “Spin dynamics and a nearly continuous magnetic phase transition in an entropy-stabilized oxide antiferromagnet,” *Physical Review Materials* **4**, 074405 (2020).
- [43] Y. Uemura, S. Lee, R. Cywinski, and S. Kilcoyne, *Muon Science: Muons in Physics, Chemistry, and Materials* (Taylor and Francis, 1999).

- [44] L. Rebbouh, R. P. Hermann, F. Grandjean, T. Hyeon, K. An, A. Amato, and G. J. Long, “Fe 57 Mössbauer spectral and muon spin relaxation study of the magnetodynamics of monodispersed γ -Fe₂O₃ nanoparticles,” *Physical Review B* **76**, 174422 (2007).